JOURNAL OF Applied Polymer SCIENCE

Characterization of the Viscoelastic Behavior of the Pure Bitumen Grades 10/20 and 35/50 with Macroindentation and Finite Element Computation

Rabah Hamzaoui,[1] Sofiane Guessasma,[2,3] Abdelkrim Bennabi[1]

[1]Université Paris-Est, Institut de Recherche en Constructibilité, Ecole Spéciale des Travaux Publics du Bâtiment et de l'Industrie (ESTP), 28 Avenue du Président Wilson, 94234 Cachan, France

[2]Institut National de Recherche Agronomique, Research Unit Biopolymères, Interactions et Assemblages, Rue de la géraudière, 44300 Nantes, France

[3]Composite and Heterogeneous Materials Analysis and Simulation Laboratory, Physical Science and Engineering Division, King Abdullah University of Science and Technology, 4700 Kaust, Thuwal 23955-6900, Saudi Arabia

Correspondence to: S. Guessasma (E-mail: sofiane.guessasma@nantes.inra.fr or sofiane.guessasma@kaust.edu.sa)

ABSTRACT: In this article, we present an identification procedure that allows the determination of the viscoelasticity behavior of different grades of pure bitumen (bitumen 35/50 and bitumen 10/20). The procedure required in the first stage a mechanical response based on macroindentation experiments with a cylindrical indenter. A finite element simulation was performed in the second stage to compute the mechanical response corresponding to a viscoelasticity model described by three mechanical parameters. The comparison between the experimental and numerical responses showed a perfect matching. In addition, the identification procedure helped to discriminate between different bitumens characterized by different asphaltene and maltene contents. Finally, the developed procedure could be used as an efficient tool to characterize the mechanical behavior of the viscoelastic materials, thanks to the quantified relationship between the viscoleastic parameters and the force–penetration response. © 2013 Wiley Periodicals, Inc. J. Appl. Polym. Sci. 130: 3440–3450, 2013

KEYWORDS: mechanical properties; properties and characterization; structure-property relations; theory and modeling; viscosity and viscoelasticity

Received 4 February 2013; accepted 23 April 2013; Published online 23 June 2013

DOI: 10.1002/app.39458

INTRODUCTION

Bitumen is a black or brown highly viscous liquid or semisolid material present in most crude oils and in some natural deposits.[1,2] It is mostly composed of hydrocarbons with a small amount of structurally analogous heterocyclic species. Bitumen may typically contains 83–86% carbon (with up to 150 carbon atoms), 9–10% hydrogen, 1–5% sulfur, less than 1% each of nitrogen and oxygen, and minor amounts of metals such as vanadium and nickel.[3–5] At low temperatures, bitumen is rigid and brittle. It becomes flexible at room temperature, and at higher temperatures, it flows.[6–8] In addition, bitumen is a colloidal system, where the highest molecular weight components, namely, the asphaltenes (As), and the lower molecular weight maltenes [aromatics (A), saturates (S), and resins (R)] are dissolved in the saturated hydrocarbon mixture, and the heteroatomic content is in this order S < A < R < As.[9–13]

Several contributions have reported the identification of the mechanical behavior of heterogeneous viscoelastic materials with different methodologies.[14–19] Indentation is usually exploited to derive the mechanical behavior of bitumen materials at different macroscales, microscales, and nanoscales.[18,20,21] However, such a test is not as simple as it may appear because the temporal evolution of the contact surface has to be properly measured to determine the true stress transfer toward the indented material. In addition, the success of indentation can be altered by boundary effects if the stress that develops is not exclusively localized around the indenter footprint.[16] As pointed out in the study of Ossa et al.,[21] adhesion between the indenter and bitumen has to be considered because it significantly influences the observed recovery behavior.

Nanoinentation is used to gain valuable information about the fine structure effect on the macroscopic response,[20] whereas macroindentation is more adequate in the case of a heterogeneous macrostructure.[21] Macroindentation is a better alternative to determine the average mechanical behavior. Indentation can address different deformation stages, ranging from elasticity to plasticity to viscous-dependent behaviors. The simultaneous identification of different deformation stages can be achieved by the decoupling of their effects on the mechanical response with, for example, double indentation techniques.[17]

The aim of this study was to develop a characterization technique for the determination of the mechanical behavior of two grades of pure bitumen (bitumen 35/50 and bitumen 10/20). In the first step, a testing procedure was developed with a cylindrical indenter that allowed us to determine the mechanical response associated with the macroindentation experiment. In the second step, a finite element (FE) simulation was performed to compute the mechanical parameters that were relevant to fit the experimental trends. The FE simulation was associated with a viscoelastic model, namely, the Maxwell model, to characterize the viscoelastic behavior of our studied bitumen. Despite the fact that the temperature significantly affected the material behavior, we limited our attention to a unique testing temperature where all of the studied bitumens were not in the glassy state. The idea of using a macroindentation experiment instead of simple uniaxial testing came from the fact that the tested bitumens were highly viscous and could not stand without the use of containers. The usual method for determining a bitumen grade is to use a standard indentation procedure to determine the penetrability versus viscoelasticity.[2,22,23] Our ambition was to use this context to extract more information with a suitable scheme that combined FE computation and an indentation experiment.

EXPERIMENTAL

Two pure bitumens of penetration grades 35/50 and 10/20 were used in this study. These were provided by Total Co. (France). According to the AASHTO T-49 ASTM D5 norm, the grade of each bitumen was determined. Table I summarizes the penetration test results at 25°C and the softening results at 5°C for both bitumens.

Optical microscopy was performed with a Leica DM 1000 microsystem. IR spectroscopy was performed at room temperature by a Thermo Scientific Nicolet IS10 instrument, and the data were analyzed with Omnic Software.

The mechanical behavior of the bitumen was determined by a PNR 21 texture analyzer from Petrotest Co. with a load cell of 100 N. The test consisted of a confined macroindentation experiment in which a cylindrical indenter was penetrated from the surface of the specimen at a constant displacement rate (here, different velocities were tried in the range 2–8 mm/s) and an acquisition rate of 50 points/s. The testing routine included penetration down to a depth of 4 mm and then a fully unloading stage by the same amount. The force–displacement diagram was monitored during testing. The chosen test body was an aluminum cylindrical rod 8 mm in diameter and 140 mm in length. Because of the viscous nature of the bitumens, all samples were contained in jars 55 mm in diameter and 35 mm in depth. The jars were then introduced and fixed in a tempering bath with a serpentine heat-exchanger tube. The temperature of the tempering bath was maintained at 25°C (Figure 1).

Table I. Test Penetration and Softening of the Studied Bitumen

Bitumen	Test penetration at 25°C	Ring and ball softening at 5°C
10/20	18.0 (1/10 mm)	72.9°C
35/50	46.7 (1/10 mm)	53.4°C

Figure 1. Sample conditioning prior testing. [Color figure can be viewed in the online issue, which is available at www.interscience.wiley.com.]

FE SIMULATION

Simulation of macroindentation was performed with ANSYS FE software. The partial geometries and dimensions all conformed to the experimental conditions. The indenter was an aluminum cylinder (partial height = 80 mm, diameter = 8 mm). Although different indenter shapes can be used, each indenter allows a particular response. For example, a Berkovich tip has a self-similarity property that makes it suitable for low-scale indentations.[14] Spherical indenters are preferred to avoid severe plastic deformation because of the larger increase in the contact surface at small depths. In our case, the cylindrical shape allowed us to consider a constant contact area but with the cost of significant shearing at the contact periphery.

The bitumen sample to be indented also had a cylindrical shape (height = 35 mm, diameter = 55 mm). All parts were meshed with consideration of the solid elements. Indenter meshing was irregular and was performed with tetrahedral solid elements (solid92), which were defined with 10 nodes, all of which were capable of structural displacements in the x, y, and z directions. The meshing of the sample part was regular with hexahedron elements (solid185) with eight nodes, also with three translations for each node in the x, y, and z directions. Despite the fact that the indenter was used as a rigid body, the elastic properties of the material could be specified in the computation. As mentioned, the indenter's material properties corresponded to an isotropic aluminum material ($E_I = 70$ GPa, $\nu_I = 0.34$, where E_I and ν_I are the Young's modulus and Poisson ratio, respectively). The bitumen material properties were examined on the basis of a viscoelastic model.[14] Such a model is realistic with regard to most published articles in the concerned literature and observed response.[20] The general framework for the constitutive equation uses elastic and viscous contributions.[24] The stress function under the small-strain viscoelasticity approximation has an integration form that handles the contribution of past distant strains:[14]

$$\sigma = \int_0^t 2G(t-\tau)\frac{de}{d\tau}d\tau + I\int_0^t K(t-\tau)\frac{d\Delta}{d\tau}d\tau \tag{1}$$

where σ is the Cauchy stress; e is the deviatoric part of the strain; Δ is the volumetric part of the strain; τ and t are the past and present times, respectively; $G(t)$ and $K(t)$ are the shear and bulk relaxation kernel functions, respectively; and **I** is the identity tensor.

We made use of the Maxwell model, assuming spring–dashpot combinations to represent the viscoelastic behavior.[25] The relaxation functions introduced in eq. (1) can be approached with the Prony series:[14]

$$X(t) = X_f + \sum_{j=1}^{n_X} X_j e(-t/\tau_j^X) \tag{2}$$

where X is either G or K, X_f is the final modulus or the modulus at slow load, n_X is the number of Maxwell elements used to approximate the kernel function associated with either the shear or bulk behavior, X_j is the initial modulus or the modulus at fast load, and τ_j^X is the relaxation time associated with each Prony component.

The Maxwell discrete relaxation spectrum could be further explicated with the additional approximation of one Maxwell element together with an isotropic hypothesis. We achieved the following reduced form:

$$X(t) = X_f + X_1 e(-t/\tau_1^X) \tag{3}$$

where X holds also for E_I.

Three main parameters were searched, namely, the instantaneous modulus $(E_i) = E_1$ [E_1 is the modulus associated to element 1 in the generalized Maxwell model. It is called here instantaneous modulus.], final Young's modulus (E_f), and the decay constant (β). These were related to each other with the following expression

$$E_M(t) = E_f + (E_i - E_f)e^{-\beta t} \tag{4}$$

where E_M is the time (t)-dependent modulus and $\beta = 1/\tau_i$.

The physical meanings of E_i and E_f were evident as these parameters represent the material elastic response at fast and slow uniaxial loadings, respectively. β is the inverse of the relaxation time associated with the Maxwell element.

The model was sufficiently accurate with only three parameters, despite the fact that the temperature was not considered here. Indeed, the temperature influenced the viscous part of bitumen and, in turn, its rheological behavior. It has been shown that Arrhenius-type dependence can be associated with the mechanical response.[20] Although temperature effects have a great influence on the mechanical behavior, our experiments were all conducted at the same temperature (i.e., room temperature).

In addition to partial meshing, a definition of appropriate contact elements was required to avoid element penetration during FE processing. Surface-to-surface contact was considered in our modeling, where target plane elements (target170) were associated with the displaced and undeformed part (i.e., the indenter) and contact elements were implemented for the deformable surface. Symmetrical contact was not considered here to avoid doubling the element number. To further reduce the number of contact pairs, the contact surface was limited to the central arrowed region shown in Figure 2, where penetration was

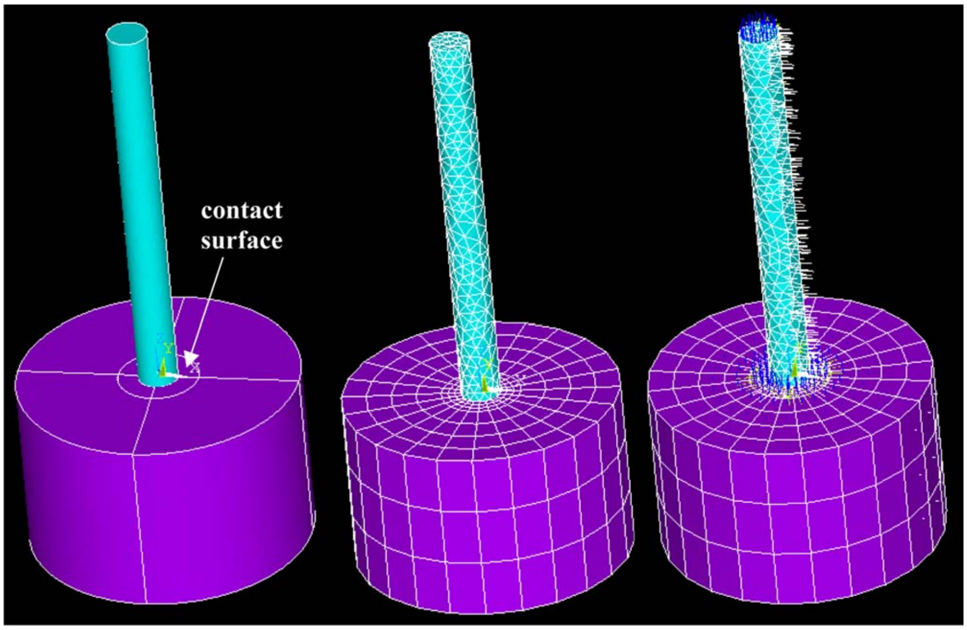

Figure 2. Partial geometry, meshing, and boundary conditions. [Color figure can be viewed in the online issue, which is available at www.interscience.wiley.com.]

expected to occur. The contact detection accuracy was not affected much because only one part was displaced. The penalty method was used for contact detection on gauss points with a friction coefficient of 0.2 and no contact cohesion at least during the loading process. The change in the friction coefficient did not seem to have particular influence on the force–depth relationship. The model size, including solid and contact elements, did not exceed 3000 elements.

The boundary conditions represent the displacement of the indenter in the z direction with a constant velocity and the following the constraints

$$\begin{cases} UX = UY = 0 \\ UZ(t) = -vt \end{cases} \tag{5}$$

where the set of expressions in eq. (5) is valid for all nodes belonging to the indenter part. UX, UY and UZ are structural displacements in space directions X, Y and Z, respectively.

The condition expressed in eq. (5) corresponds to a rigid vertical displacement of the indenter. The mold part obeyed the following constraints:

$$UX = UY = UZ = 0 | x^2 + y^2 = R^2 \quad \text{or} \quad z = z_{\min} \tag{6}$$

where R is the radius of the cylindrical holder and $z = z_{\min}$ corresponds to the holder base.

In eq. (6), the indented material is contained in a cylindrical form to simulate the container reaction.

Postprocessing included a comparison between the numerical and experimental force–depth of penetration curves. An error function was first defined and then decreased on the basis of the adjustment of the model parameters (E_i, E_f, and β). This error function, named here an objective function, was to be minimized. We can write

$$g = \frac{1}{N} \sum_{i=1}^{N} |F^{EXP}(UZ_i) - F^{NUM}(UZ_i)| / F^{EXP}(UZ_i) \tag{7}$$

where g is the objective function, superscripts EXP and NUM refer to experimental and numerical, respectively, F and UZ are the force and depth of penetration, respectively, and N is the number of imposed displacement increments or load steps.

The process of minimization was based on a regular sieving in the space of parameters giving adequate bounds. Despite the fact that different automated inverse strategies are more reliable,[15] the use of adequate bounds for parameters E_i, E_f, and β decreased the time spent searching for a global solution. Adequate bounds were chosen so that trials on the search domains produced small g values. At this stage, a sieving search was applied on the selected search domain. In the sieving method, combinations were selected regularly with a constant step size in the search domain where the objective function was evaluated. The combination was stored when it decreased g. The final stored combination corresponded to the optimal choice of considered mechanical parameters. The global optimized value of g was only achieved when close optimal g values were the result of close combinations. Each combination corresponded to one FE run that took less than 1 min on a workstation equipped with a quad-core processor.

RESULTS AND DISCUSSION

The Bitumen heterogeneous microstructure revealed with optical microscopy is depicted in Figure 3, where the spatial distribution of asphalethene and maltene of the studied bitumens 10/20 and 35/50 are shown. Asphaltene is a high-molecular-weight component appearing as a dark, solid, aggregated phase embedded in a continuous maltene matrix. The asphaltene molecule is typically composed of 10 or more fused aromatic and naphthenic rings with a significant number of alkyl side chains. Generally, the higher the asphaltene percentage is, the harder the bitumen is.[1,26] The heterogeneous maltene phase has a lower molecular weight and exhibits different compositions of A, S, and R. The A oils consist mainly of carbon, hydrogen, and sulfur with a minor amount of nitrogen and sulfur and have a molecular weight of 500–900. Saturated oils are composed of long-chain saturated hydrocarbons with some branched chain compounds and cyclic paraffins. R are composed of heterogeneous polar compounds with a small percentage of oxygen, nitrogen, sulfur, and metals.[1,3,4]

Figure 4 shows the IR absorption spectra of bitumens 35/50 and 10/20 at room temperature. Several bands are clear in the spectra. Table II shows the typical absorbance results with IR spectroscopy. These results clearly discriminate the hydrocarbon chemical family of the considered pure bitumens. According to Bukka et al.,[27] the bands at 2924 and 1376 cm^{-1} were characteristic of C—H asymmetrical stretching and C—H deformation, respectively, in —CH_3; the two bands at 2856 and 1460 cm^{-1} were associated with C—H asymmetrical stretching and C—H deformation, respectively, in —CH_2. Also, the bands at 1702, 1601, 1029, 812, and 747 cm^{-1} were characteristic of C—O stretching in carboxylic acids, C=C stretching/skeletal ring vibrations, C—O—H deformation, two adjacent C—H groups on the aromatic ring, and four adjacent C—H groups on the aromatic ring, respectively. Chaala et al.[28] have reported that the bands at 2880–2990 cm^{-1} were associated with terminal —CH_3 groups. Other bands due to alkyl chains were found at 1465 and 1380 cm^{-1} (C—H deformation), and a doublet was found at 725 cm^{-1} [—$(CH_2)_n$— skeletal vibrations].

Figure 5 shows the experimental force–depth of penetration curves for the two studied bitumens. Each curve followed a parabolic increase that could be approached with a simple polynomial function of the form:

$$F(UZ) = P_1(UZ) + P_2(UZ)^2 + P_3(UZ)^3 + P_4(UZ)^4 \tag{8}$$

where UZ is the depth of penetration and the P values are fitting parameters that are summarized in Table III for each testing condition.

The fitting of these curves with fourth-order polynomial functions was obtained with an excellent correlation factor ($R^2 > 0.99$).

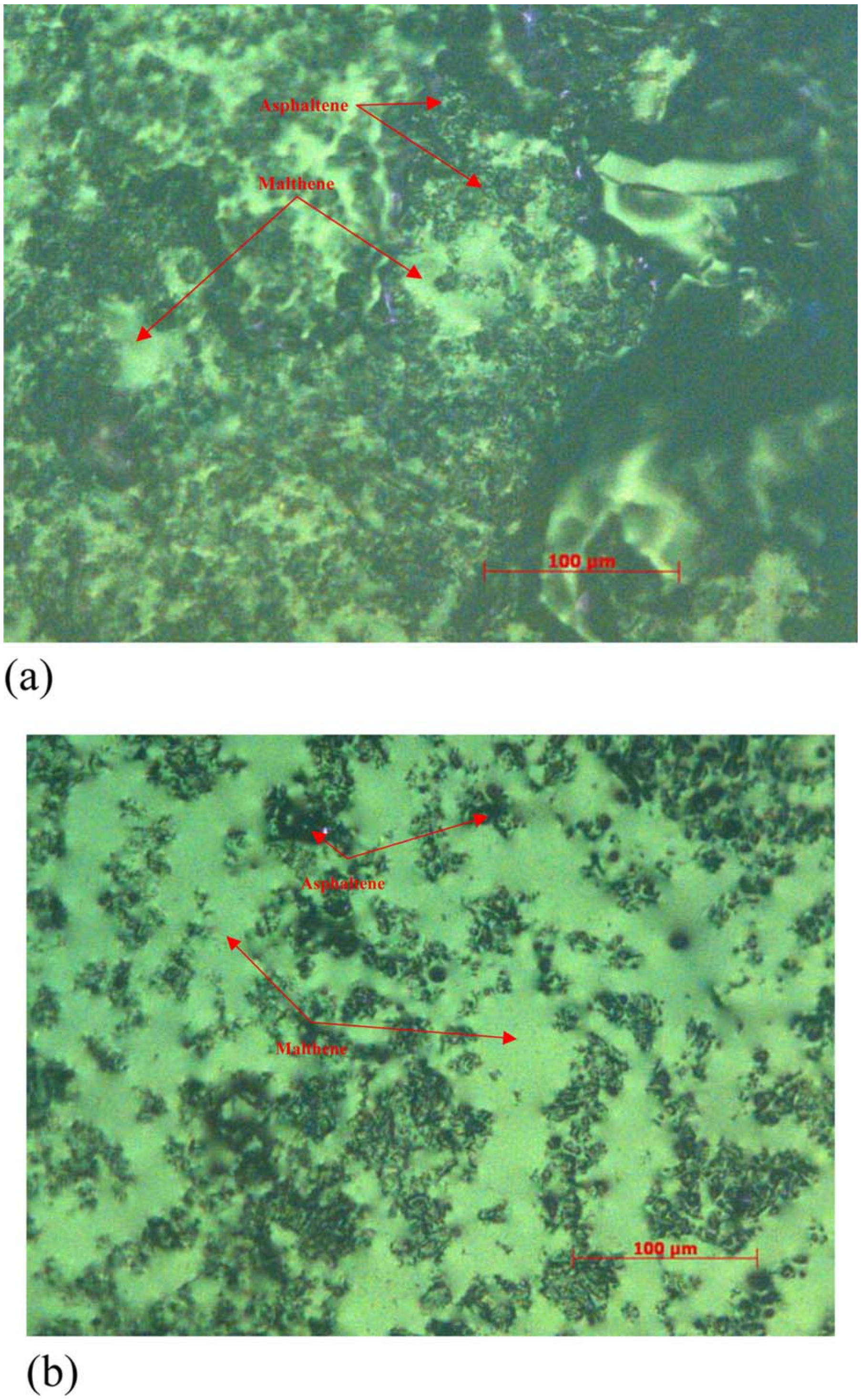

Figure 3. Microstuctures of the considered bitumens as revealed with optical microscopy: bitumen grades (a) 10/20 and (b) 35/50. [Color figure can be viewed in the online issue, which is available at www.interscience.wiley.com.]

The influence of the displacement rate was minor in the case of bitumen 10/20 [Figure 5(a)], whereas this effect was at a maximum for bitumen 35/50 [Figure 5(b)]. A large displacement velocity did not favor the viscous part of bitumen in contributing to the mechanical response. As shown in Figure 5(b), this resulted in a larger structural resistance. This result was in accordance with the fact that bitumen 10/20 had practically double the content of asphaltene than bitumen 35/50. Indeed, the higher the asphaltene percentage was, the harder the bitumen was.

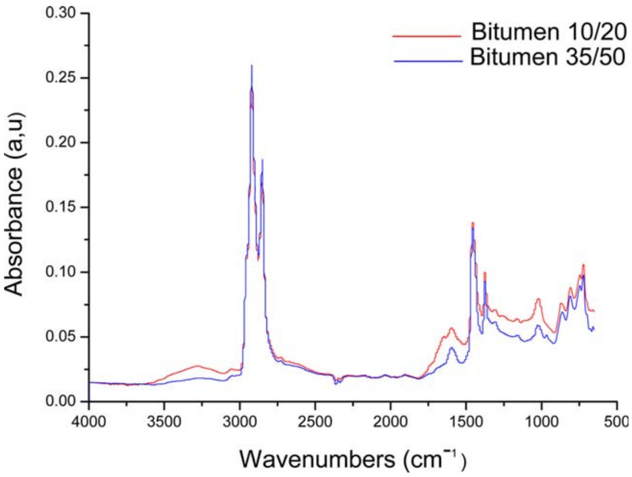

Figure 4. IR absorption spectra of bitumens 10/20 and 35/50 at room temperature. [Color figure can be viewed in the online issue, which is available at www.interscience.wiley.com.]

We observed here that the use of a viscoelastic model was meaningful in determining the mechanical behavior of the bitumens. Figure 6 shows typical nodal solutions corresponding to one experimental condition. Macroindentation with a cylindrical indenter resulted in a constant contact area and a significant shearing effect, as shown in Figure 6. In this figure, both perspective and cross-sectional views are depicted. Figure 6(a) illustrates the *z*-displacement field that developed as a consequence of *z*-displacement imposed on the indenter. We noticed a localization of the displacement field around the footprint, where the region affected by major displacement represented 45% of the total holder diameter, and its depth was about 60% of the total vertical dimensions. Such an extent of the affected zone necessarily led to boundary effects in the sense that deformation and stress were not confined to the footprint area. As expected, the displacement profile was circular at the surface and elliptical in depth. Both the mechanical strain and stress were linearly proportional to each other because the plasticity was not implemented in our model [Figure 6(b,c)]. At the contact area, compressive stresses developed but at closer locations, positive stress did exist because of the constraints added on the boundaries. The contact pressure that prevented material interpenetration was larger at the contact surface, especially in the contact edges [Figure 6(d)]. The contact area did not evolve during indentation. The constant contact area then had a direct consequence on the force–depth of penetration profile, as shown later.

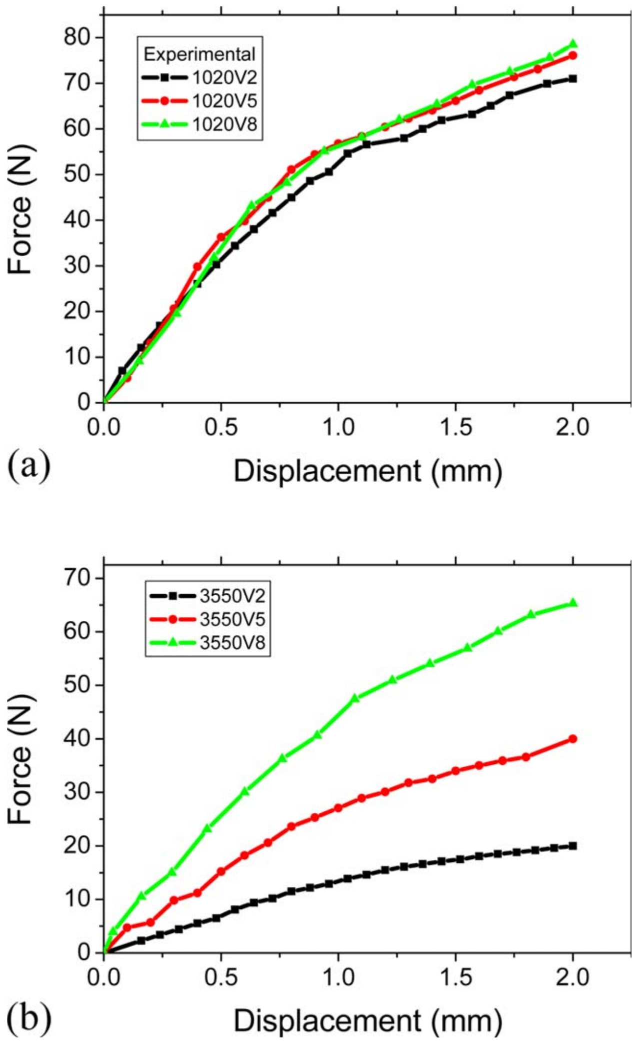

Figure 5. Experimental indentation response for bitumens (a) 10/20 and (b) 35/50. [Color figure can be viewed in the online issue, which is available at www.interscience.wiley.com.]

Table II. Absorbance Results Obtained with IR Spectroscopy

Wave number (cm^{-1})	Attribution of main absorption bands
722	$\delta_r(CH_2)_n$, $n > 4$
745	ω (4H adjacent to aromatic ring)
809 and 862	δC—H in substituted A
1032	ν S=O
1172 and 1191	C—O—C of the aliphatic ester
1312	—CH=CH— stretching and deformation vibrations
1376	$\delta(CH_3)$ due to CH_3 terminal groups on fatty ester chains
1458	$\delta(CH_2)$
1586	C=C in-plane vibrations
1605	—NH_2 deformation
2851 and 2920	ν (CH_2)

Sensitivity Analysis

Part of the nodal solutions was the prediction of the reaction force that the material exerted on the indenter. The sum of the *z* component of all of the nodal reaction forces was related to the depth of penetration. It was thus interesting to study how the viscoelastic parameters affected the mechanical response. Figure 7 shows the effect of E_i on the mechanical response. The other viscoelastic parameters were selected to have reaction

Table III. Sample Conditions and Related Experimental and Numerical Mechanical Parameters

		Fitting response					Viscoelastic parameters			
Number	Bitumen	P_1	P_2	P_3	P_4	R^2	E_i (MPa)	E_f (MPa)	β (—)	g (—)
B1020V2	10/20	74	−19.00	−6.22	3.06	0.999	12.00	1.00	9.10	0.023
B1020V5		75	−0.06	−27.39	9.16	0.998	12.00	1.00	8.6	0.025
B1020V8		68	12.20	−33.36	10.13	0.998	13.00	1.00	9.10	0.024
B3550V2	35/50	12	6.96	−7.75	1.82	0.999	2.50	0.01	5.00	0.036
B3550V5		30	8.31	15.09	4.25	0.998	6.00	1.00	9.60	0.032
B3550V8		61	−18.49	1.96	0.17	0.999	10.00	1.00	8.60	0.011

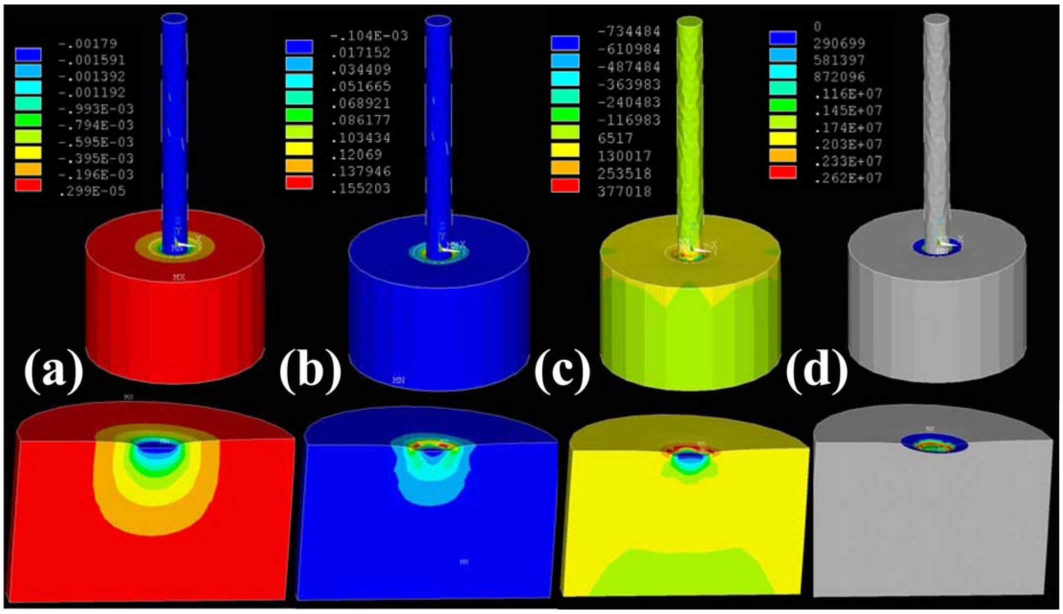

Figure 6. Example of the nodal solutions: (a) z displacement, (b) mechanical strain, (c) principal stress, and (d) contact pressure (E_i = 10 MPa, E_f = 0.5 MPa, and β = 4). [Color figure can be viewed in the online issue, which is available at www.interscience.wiley.com.]

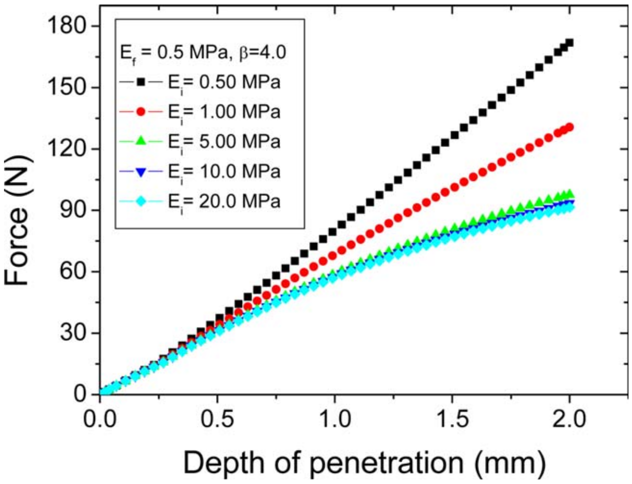

Figure 7. Sensitivity analysis: effect of E_i on the force–depth of the penetration relationship. [Color figure can be viewed in the online issue, which is available at www.interscience.wiley.com.]

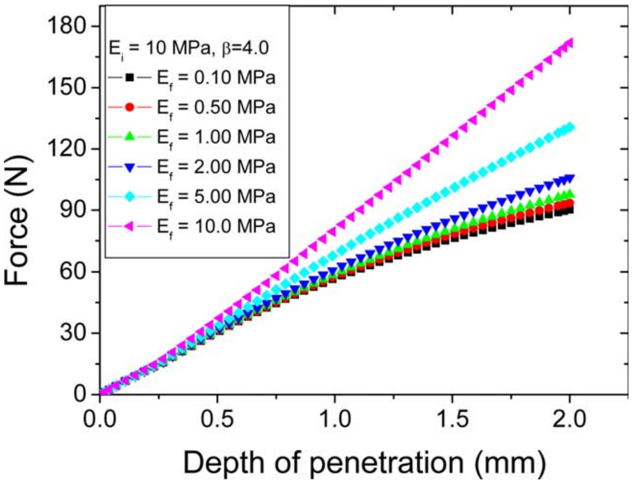

Figure 8. Sensitivity analysis: effect of the final modulus on the macroindentation response. [Color figure can be viewed in the online issue, which is available at www.interscience.wiley.com.]

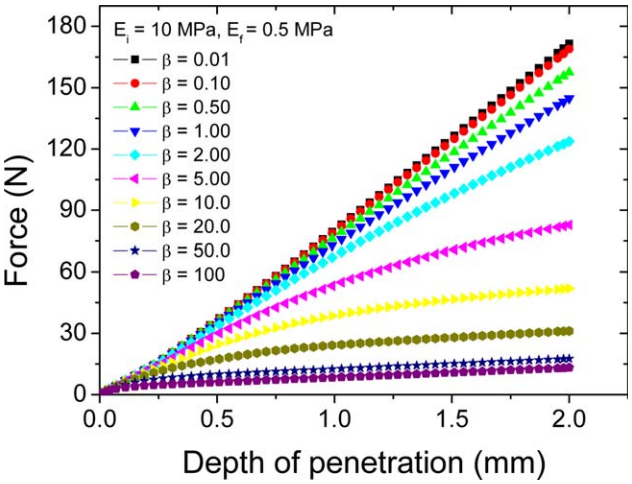

Figure 9. Sensitivity analysis: effect of β on the macroindentation response. [Color figure can be viewed in the online issue, which is available at www.interscience.wiley.com.]

forces comparable to the observed trends (Figure 5). Within the range 0.5–20 MPa, we noticed a highly nonlinear effect of E_i on the mechanical response. When this parameter was equal to the final modulus ($E_i = E_f$), a linear trend was predicted, which confirmed a linear elastic behavior. When E_i was greater than E_f, the stress relaxation prevailed because of the viscous component of the material. Lower reaction forces were observed together with a parabolic behavior. Minor changes in the mechanical response occurred when E_i was greater than 5 MPa.

Figure 8 shows that the effect of the final modulus was similar to that of E_i, with the exception that a decrease in the reaction force was obtained with the decrease in E_f. We assumed at this stage that the macroindentation response depended on the ratio E_f/E_i.

Figure 9 depicts the effect of β on the mechanical response. This parameter measures how fast the modulus should reach its final value starting from the instantaneous level. It clearly tuned the time dependence of E_I, as shown in Figure 9, where the modulus loss was utmost when β was large. β modified the mechanical response from a linear shape ($\beta < 1.0$) to a steady-state regime ($\beta > 10$). Thus, the selection of an appropriate β value for the observed trends would necessarily be based on the shape of the experimental response. The rough analysis of trends reported in Figure 5 suggests that $\beta > 1$ when the instantaneous and final moduli were close to the values given in Figure 9.

We noticed also that all of the viscoelastic parameters had similar effects on the force–depth of penetration as long as we observed, in all cases, a transition from linear to nonlinear trends, depending on the range of selected values. Parameter interdependencies with regard to the profile of the mechanical response would require testing of all possible E_i, E_f, and β combinations to derive appropriate correlations between the mechanical response and constitutive law. For such purposes, the viscoelastic parameters were combined within the bounds detailed in Table IV. Under these conditions and with the knowledge that $E_f \leq E_i$, up to 1225 FE runs were performed. All of the predicted responses were fitted with the polynomial function [eq. (8)], the and fitting parameters (P's) were related to the viscoelastic parameters.

Table IV. Range of Variation and Sampling Steps in the Space of the Viscoelastic Parameters

	Minimum	Maximum
E_i	0.5	20
E_f	0.01	11
β	0.01	100

Table V. Fitting Parameters Relating the Macroindentation Response to Viscoelastic Constitutive Law

	a	b	c	d	R^2
P_1	5.89	−0.15	0.11	−0.53	1.00
P_2	0.68	3.36	−3.06	14.51	0.83
P_3	−1.35	−0.79	1.13	−5.40	0.88
P_4	0.34	0.08	−0.16	0.75	0.91

Using automated fitting routines, all of the coefficients (P's) displayed linear tendencies of the form

$$P_i = a_i E_0 + b_i E_\infty + c_i \beta + d_i \tag{9}$$

where E_i and E_f are instantaneous and final modulii, respectively, β is a decay constant, i refers to the index of the polynomial coefficients in eq. (8) and a_i, b_i, c_i, and d_i are new coefficients that express the correlations between the P values and the viscoelastic parameters.

As shown in Table V, all of the fitting quantities were predicted with an acceptable correlation factor ($R^2 > 0.82$). Figure 10 compares the P coefficients, where the data on x axis refer to the resulting P's fitted from the FE results, and the data on the y axis represent the fitting results found with eq. (9). Perfect matching required that all circles lie on the bisector line. In our case, the best result was obtained for P_1.

Identification of Observed Mechanical Behavior

Taking advantage of the sensitivity analysis, we show the viscoelastic parameters determined for each experimental trend in Figure 5. For such purposes, the size of the database was enlarged to have a more precise resolution in the space of the mechanical parameters. This database thus contained 2315 parameter combinations for which macroindentation responses were known. For the next stage, we needed an inverse strategy to derive the optimal viscoelastic parameters. All of the combinations that decreased the objective function [eq. (7)] were sorted out, as shown in Figure 11. In this example, we noticed that β highly fluctuated because, at the beginning of the process, the steepness of the curve had no major influence on the convergence compared to the elastic moduli (E_i and E_f). Both E_i and E_f decreased to lower the objective function; this indicated

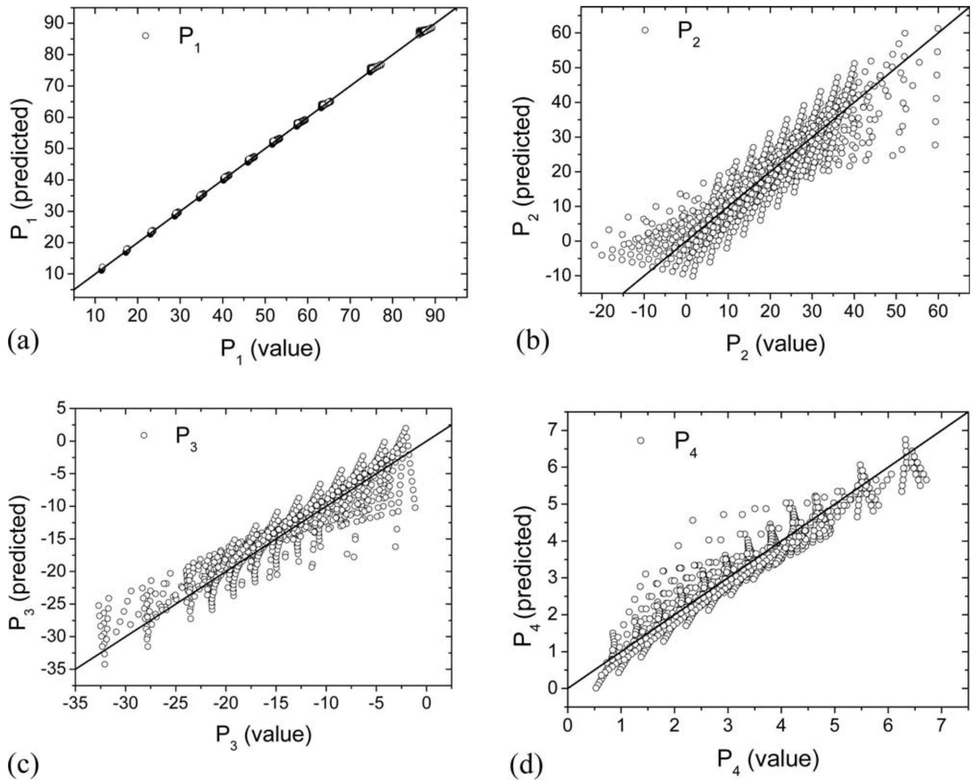

Figure 10. Comparison between the predicted and fitted P coefficients as issued from the FE computations and fitting routines, respectively.

that control of the magnitude of the force prevailed. The final optimal combination was obtained by an adjustment of β to match the steady-state part of the experimental response.

Figure 12(a) shows a comparison of the FE and experimental responses for different values of the objective function corresponding to the case treated in Figure 11. The choice of the form of the objective function was critical for achieving the best matching between the numerical and experimental responses. The relative error form in the g expression [eq. (7)] led to numerical curves that were closer to the experimental response when g decreased. As shown in this figure, perfect matching was reached at the final stage when g was equal to 0.03. The optimization process was repeated for the other experimental conditions, and the optimal configurations were compared with the experimental conditions. Figure 12(b) shows that the viscoelastic model truly represented the experimental behavior as long as a decrease in g was possible. Table III summarizes the optimal mechanical parameters for each experimental condition. The predicted E_i was correlated here with the stiffness of the material, which was in turn related to the elastic component of the material behavior. It is well understood that such components appear for any viscoelastic materials at fast loading rates. The predicted E_i values were larger for bitumen grade 10/20; this indicated that such a bitumen was stiffer compared to grade 35/50. This result was consistent with test penetration results reported in Table I. In addition, different values of E_i values were predicted for grade 35/50; this indicated that one Maxwell element was not sufficient for fully determining the viscoelastic properties of such a bitumen. The final moduli were significantly lower than the E_i values for both grades. The E_i/E_f ratio was thus quite large as it evolved between 6 and 250. The upper bound of such a ratio was reached for sample B3550V2. To conclude, on the viscous part of each bitumen, we had to examine the relaxation times for each grade. In most cases, a large β was predicted ($\beta \geq 5.0$); this means that small relaxation times were associated with the predicted behavior. We use the term *large* here to be in line with the observed parabolic shapes shown in Figure 9. On the average, grade 10/20 exhibited a larger β of about 8.93 ± 0.29 compared to grade 35/50 (7.73 ± 2.42). This result highlights the different viscous properties of the studied bitumens, as bitumen 10/20 exhibited a fast modulus relaxation compared to bitumen 35/50. In the last situation, the results were obtained with a large standard deviation of 31% compared to bitumen 10/20 (3%). This meant that the behavior of bitumen 35/50 under low and fast loadings was completely inhomogeneous.

So, the sensitivity of the viscoelastic parameters with regard to the considered samples showed that the viscoelastic properties were more stable for bitumen 10/20 ($E_i/E_f \approx 12$), whereas for bitumen 35/50, the change was significant [$E_i/E_f \in (6250)$]. One Maxwell element was relevant in the case of bitumen 10/20, which appeared here to be less viscous and stiffer compared to bitumen 35/50.

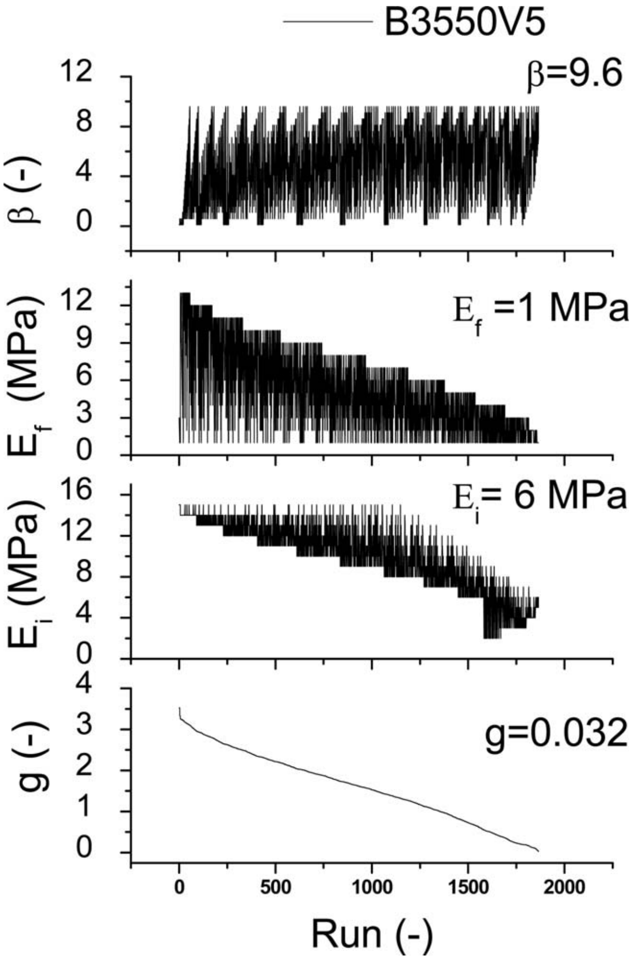

Figure 11. Example of the inverse process to determine the viscoelastic parameters based on the experimental trend and FE computation.

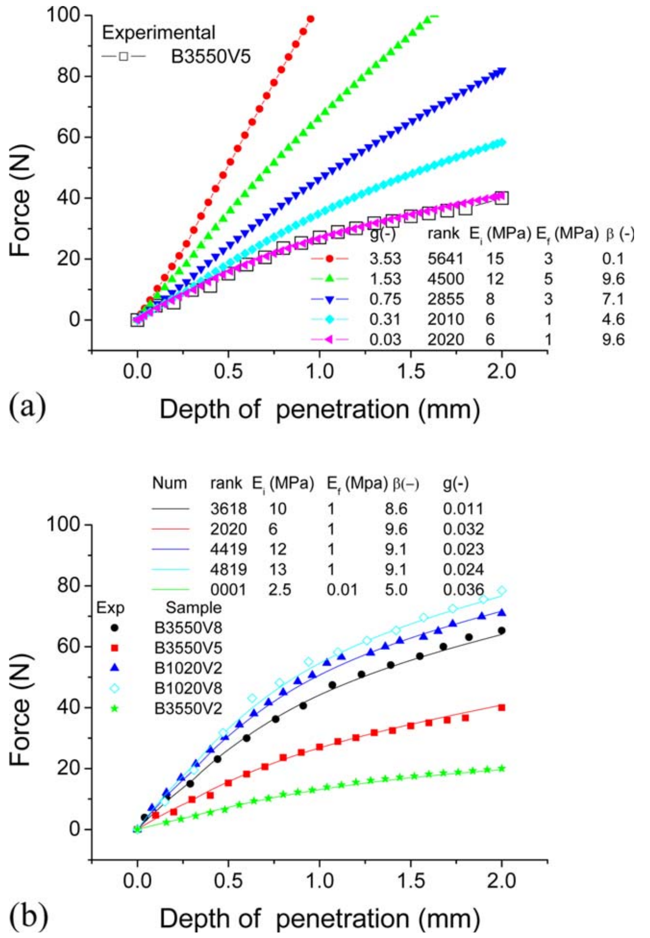

Figure 12. (a) Typical optimization process leading to perfect matching between the experimental and numerical curves. (b) Comparison between the experimental and numerical trends for different bitumens. [Color figure can be viewed in the online issue, which is available at www.interscience.wiley.com.]

CONCLUSIONS

The viscoelastic properties of bitumen were approached with an identification procedure that combined FE computation and macroindentation experiments. The viscoelastic model used a simple Maxwell model, where three variables had to be determined, namely, β and the instantaneous and final moduli. The sensitivity analysis showed the nonlinear relationships between the predicted mechanical trends and the viscoelastic parameters well. The parabolic shape of the force–displacement response was predicted for either large E_i or small final modulus values. The nonlinearity of the macroindentation response depended thus on the ratio of the former quantities. When both quantities were equal, a linear response was predicted. A large decay had a similar parabolic effect on the mechanical trends. A simple linear relationship was derived between fitting coefficients associated with the observed mechanical behavior and the viscoelastic parameters. The identification results highlighted the advantage and limitations of using a simple Maxwell model described by only three parameters. The model was able to discriminate both tested grades. The achieved parameters indicated that bitumen 10/20 was stiffer and less viscous than bitumen 35/50 with regard to the higher E_i and small relaxation duration. For grade 35/50, a better identification of the viscoelastic behavior would require a larger number of Maxwell elements.

REFERENCES

1. Parkash, S. Petroleum Fuels Manufacturing Handbook Including Specialty Products and Sustainable Manufacturing Techniques; McGraw-Hill: New York, NY; **2010**.
2. Vasiljevic-Shikaleska, A.; Popovska-Pavlovska, F.; Cimmino, S.; Duraccio, D.; Silvestre, C. *J. Appl. Polym. Sci.* **2010**, *118*, 1320.
3. Read, J.; Whiteoak, D. The Shell Bitumen Handbook; Thomas Telford: London; **2003**.
4. Hefer, A.; Little, D. Report Number ICAR/505-1; Texas A&M University System: Springfield, Virginia; **2005**, 220 pp.
5. Stangl, K.; Jäger, A.; Lackner, R. *Monatshefte Chem.* **2007**, *138*, 301.
6. Navarro, J.; Partal, P.; Garcıa-Morales, M.; Martın-Alfonso, M.; Martınez-Boza, F.; Gallegos, C.; Bordado, J.; Diogo, A. *J. Ind. Eng. Chem.* **2009**, *15*, 458.

7. Yousefi, A. *Prog. Color Colorants Coat.* **2008**, *1*, 45.
8. Masson, J.; Polomark, G. *Thermochim. Acta* **2001**, *374*, 105.
9. Zhang, J.; Wang, J.; Wu, Y.; Sun, W.; Wang, Y. *Iranian Polym. J.* **2009**, *18*, 465.
10. Jimhez-Mateos, J.; Luis Carlos, Q.; Carmen, R. *Fuel* **1996**, *75*, 1691.
11. Garcia-Morales, M.; Partal, P.; Navarro, F.; Martınez-Boza, F.; Gallegos, C.; Gonzalez, N.; Gonzalez, O.; Munoz, M. *Fuel* **2004**, *83*, 31.
12. Lesueur, D. *Adv. Colloid Interface Sci.* **2009**, *145*, 42.
13. Loeber, L.; Muller, G.; Morel, J.; Sutton, O. *Fuel* **1998**, *77*, 1443.
14. Guessasma, S.; Sehaki, M.; Lourdin, D.; Bourmaud, A. *Comput. Mater. Sci.* **2008**, *44*, 371.
15. Buljak, V. *FME Trans.* **2010**, *38*, 129.
16. Passeri, D.; Bettucci, A.; Biagioni, A.; Rossi, M.; Alippi, A.; Tamburri, E.; Lucci, M.; Davoli, I.; Berezina, S. *Ultramicroscopy* **2009**, *109*, 1417.
17. Jager, A.; Lackner, R. *Strain* **2009**, *45*, 45.
18. Gouldstone, A.; Chollacoop, N.; Dao, M.; Li, J.; Minor, A. M.; Shen, Y.-L. *Acta Mater.* **2007**, *55*, 4015.
19. Vanlandingham, M. R.; Chang, N.-K.; Drzal, P. L.; White, C. C.; Chang, S.-H. *J. Polym. Sci. Part B: Polym. Phys.* **2005**, *43*, 1794.
20. Jäger, A.; Lackner, R.; Eberhardsteiner, J. *Meccanica* **2007**, *42*, 293.
21. Ossa, E. A.; Deshpande, V. S.; Cebon, D. *Acta Mater.* **2005**, *53*, 3103.
22. Fawcett, A. H.; Mcnally, T. M. *J. Appl. Polym. Sci.* **2000**, *76*, 586.
23. Singh, B.; Kumar, L.; Gupta, M.; Chauhan, G. S. *J. Appl. Polym. Sci.* **2013**, *127*, 67.
24. Phan-Thien, N., Understanding Viscoelasticity: An Introduction to Rheology; Springer: Berlin, Heidelberg; **2013**.
25. Ovaert, T. C.; Kim, B. R.; Wang, J. *J. Ann. Prog. Org. Coat.* **2003**, *47*, 312.
26. Durand, M.; Mouret, A.; Molinier, V.; Féron, T.; Aubry, J. M. *Fuel* **2010**, *89*, 2729.
27. Bukka, K.; Miller, J. D.; Oblad, A. G. *Energy Fuels* **1991**, *5*, 333.
28. Chaala, A.; Ciochina, O. G.; Roy, C. *Resour. Conservation Recycling* **1999**, *26*, 155.